Supporting Information

Highly active and stable surface structure for oxygen evolution reaction originating from balanced dissolution and strong connectivity in $BaIrO_3$ solid solutions

Shigeto Hirai[a]*, Shunsuke Yagi[b], He-Chan Oh[a], Yoshiki Sato[a], Wei Liu[b], En-Pei Liu[c], Wei-Tin Chen[c,d], Akira Miura[e], Masanori Nagao[f], Tomoya Ohno[a], and Takeshi Matsuda[a]

[a] School of Earth, Energy and Environmental Engineering, Kitami Institute of Technology, 165 Koen-cho, Kitami 090-8507, Japan.

[b] Institute of Industrial Science, The University of Tokyo, 4-6-1 Komaba Meguro-ku, Tokyo 153-8505, Japan.

[c] Center for Condensed Matter Sciences and Center of Atomic Initiative for New Materials, National Taiwan University, Taipei 10617, Taiwan.

[d] Taiwan Consortium of Emergent Crystalline Materials, Ministry of Science and Technology, Taipei 10622, Taiwan.

[e] Graduate School of Chemical Sciences and Engineering and Faculty of Engineering, Hokkaido University, Sapporo 060-8628, Japan.

[f] University of Yamanashi, 7-32 Miyamae, Kofu, Yamanashi 400-0021, Japan.

* Corresponding author: e-mail hirai@mail.kitami-it.ac.jp

Supplementary Results

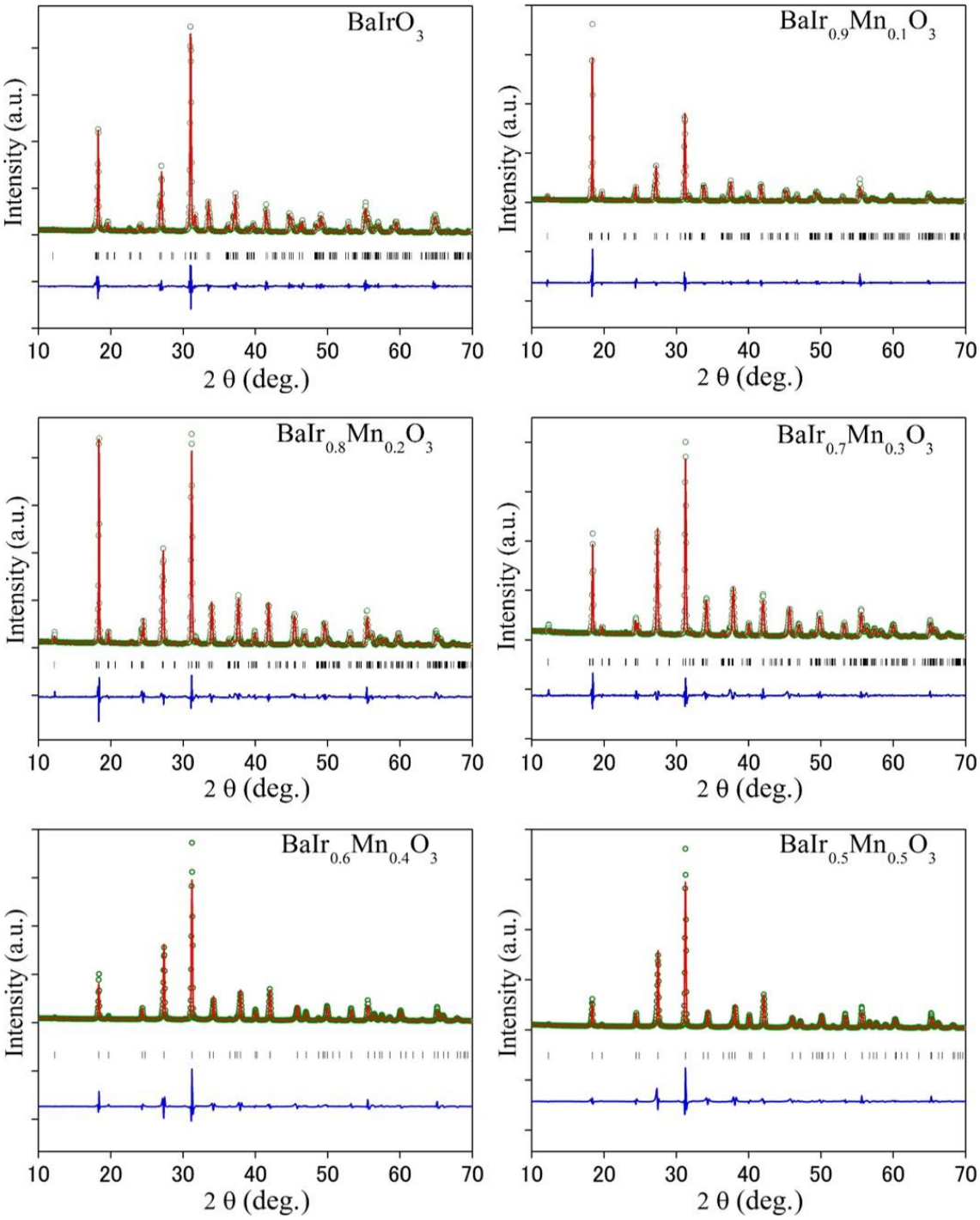

Fig. S1. XRD profiles and Rietveld refinement results of $BaIr_{1-x}Mn_xO_3$. The green circles and the red line indicate the observed and calculated profile, respectively. The blue line displays the difference between the observed and calculated profile. The black tick marks indicate the Bragg reflection positions of $BaIr_{1-x}Mn_xO_3$. Wavelength λ = 1.540598 Å.

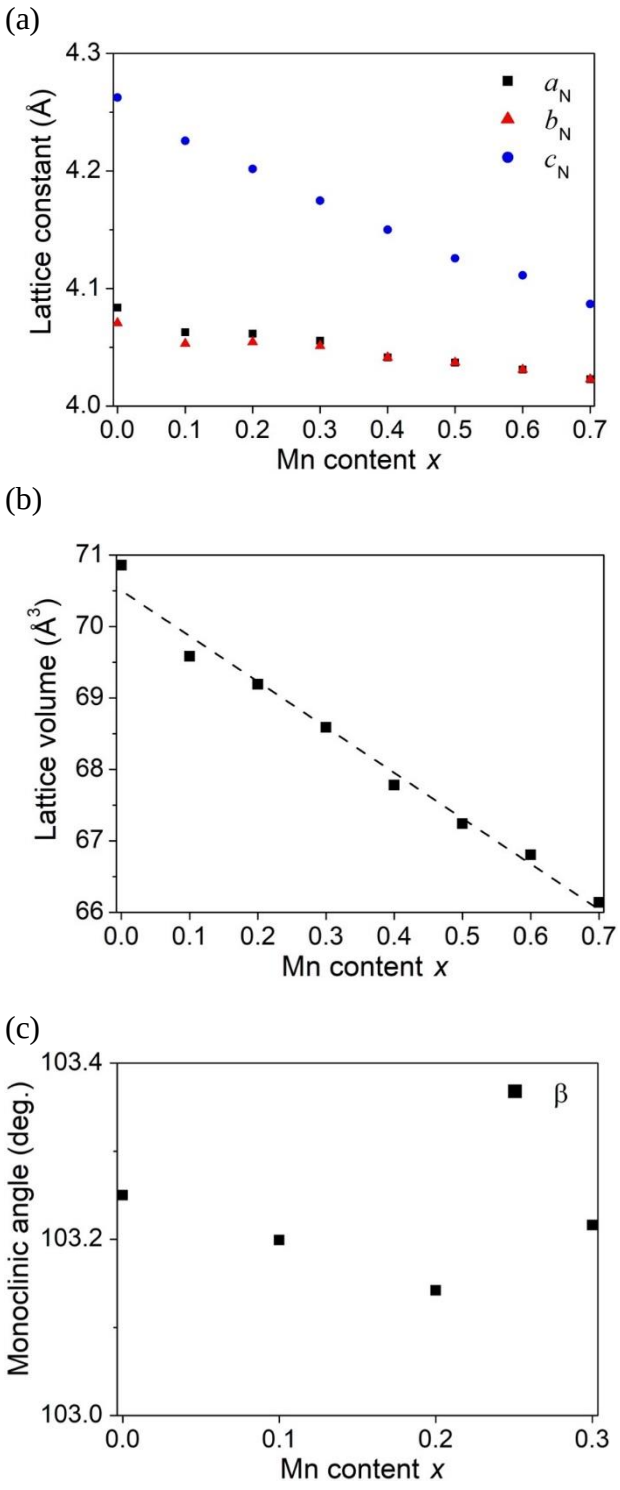

Fig. S2. Lattice constants of $BaIr_{1-x}Mn_xO_3$. (a, b, c) Evolution of the normalized lattice parameter a_N, b_N, c_N, lattice volume per chemical formula unit (V_N) and the monoclinic β angle for $BaIr_{1-x}Mn_xO_3$. The dashed line is a guide for the linear relationship between V_N and Mn content. Standard deviation for the data is within the symbol size.

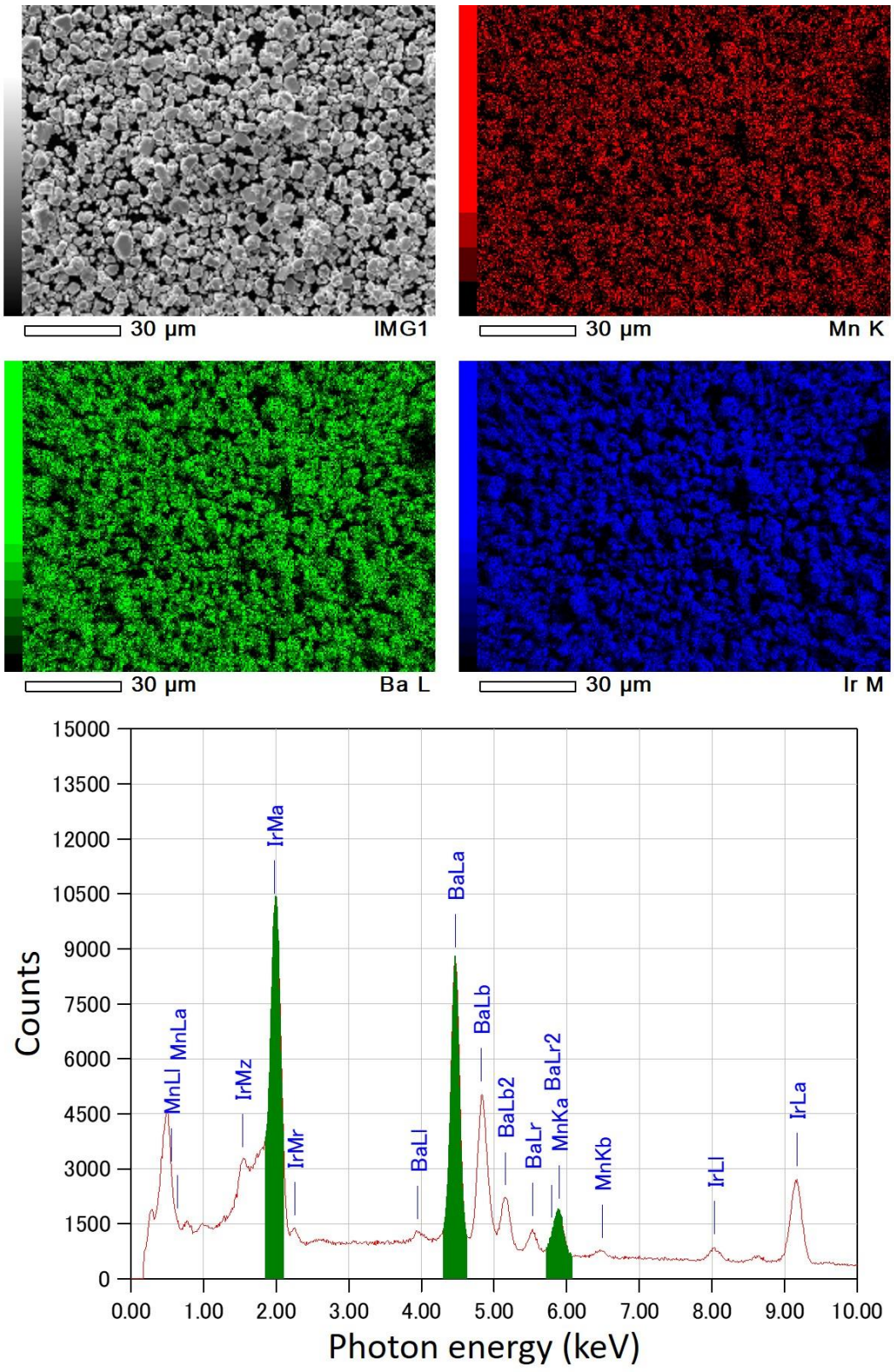

Fig. S3. SEM image and EDX mapping of $BaIr_{1-x}Mn_xO_3$. The representative SEM image, EDX elemental mapping, and EDX spectrum of $BaIr_{1-x}Mn_xO_3$ (x = 0.2).

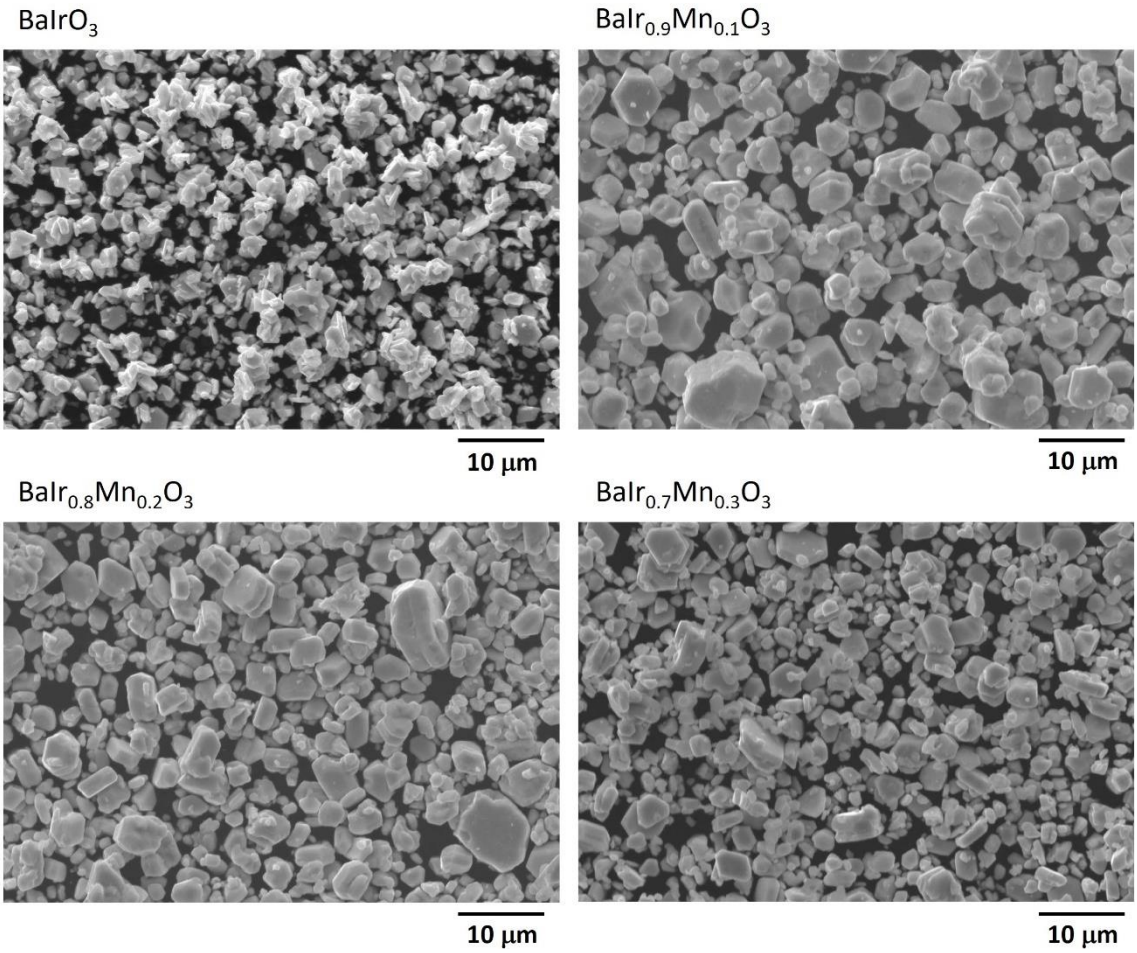

Fig. S4. SEM images of $BaIr_{1-x}Mn_xO_3$ (x = 0, 0.1, 0.2, and 0.3).

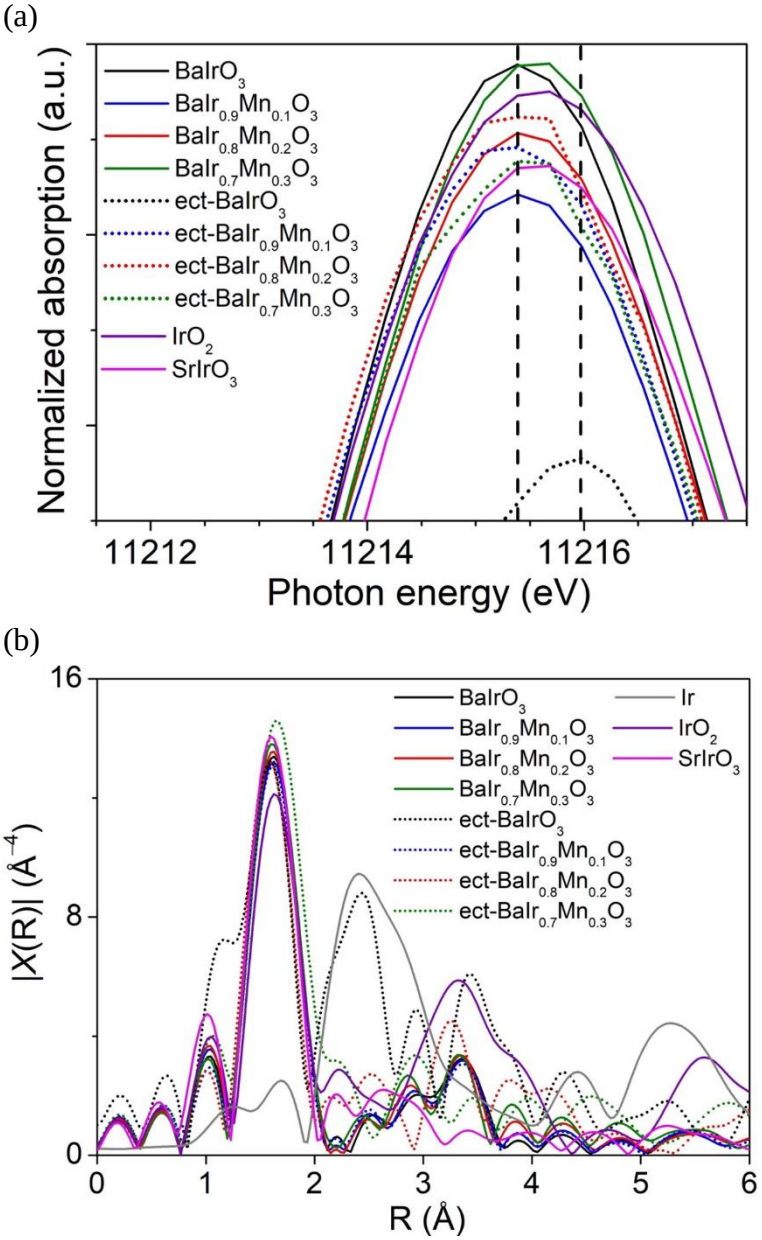

Fig. S5. Ir L_{III}-edge X-ray absorption near-edge structure (XANES) and extended X-Ray absorption fine structure (EXAFS) spectra for $BaIr_{1-x}Mn_xO_3$. (a) Expansion of the Ir L_{III}-edge white line of pristine and electrochemically treated (ect-) $BaIr_{1-x}Mn_xO_3$ (x = 0, 0.1, 0.2, and 0.3) in Figure 3f. The Ir L_{III}-edge white line of electrochemically treated $BaIr_{1-x}Mn_xO_3$ shows either a stronger peak intensity or a slight energy shift with respect to pristine $BaIr_{1-x}Mn_xO_3$. Therefore, Ir^{4+} is partially oxidized to Ir^{5+} during the OER cycling. (b) Fourier transformed k^3-weighted Ir L_{III}-edge EXAFS for pristine and electrochemically treated (ect-) $BaIr_{1-x}Mn_xO_3$ (x = 0, 0.1, 0.2, and 0.3) in the representation form of $|X(R)|$.

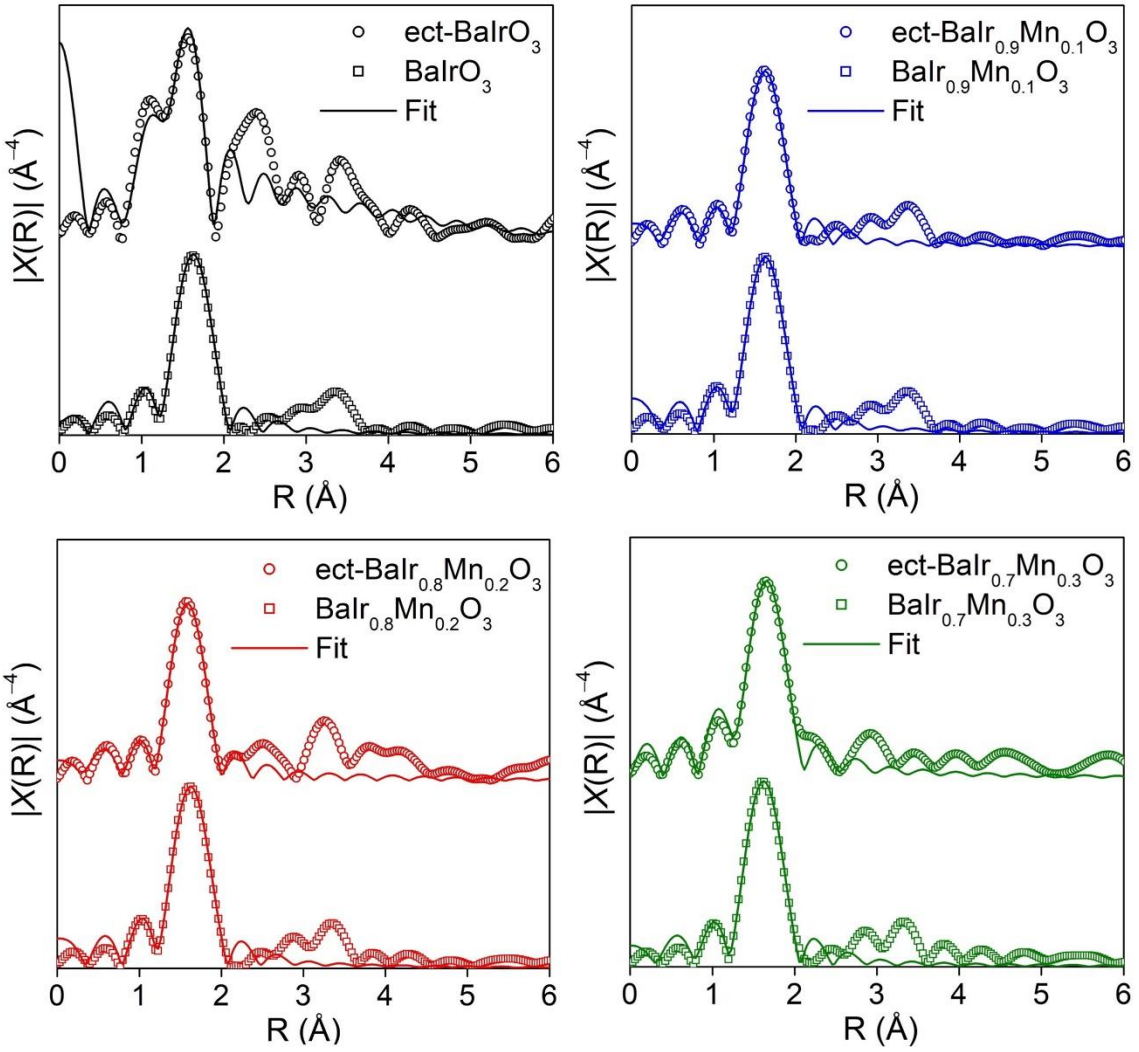

Fig. S6. Fourier transformed k^3-weighted Ir L_{III}-edge EXAFS fitting for pristine and electrochemically treated (ect-) $BaIr_{1-x}Mn_xO_3$ (x = 0, 0.1, 0.2, and 0.3) in the representation form of $|X(R)|$. A first shell was applied for the fitting. The fitting range was 2.8−10.8 $Å^{-1}$ in k-space, and 1.1−2.1 Å in R-space, respectively.

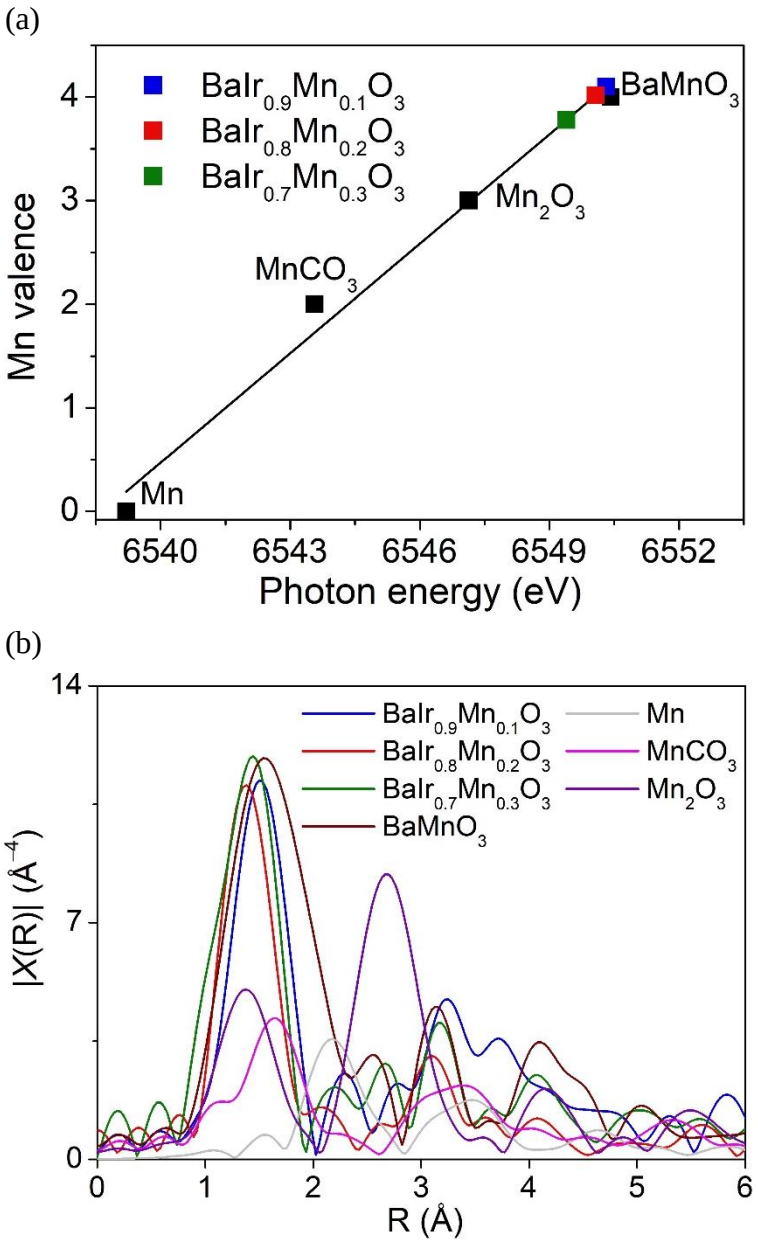

Fig. S7. Mn K-edge X-ray absorption near-edge structure (XANES) spectra for $BaIr_{1-x}Mn_xO_3$. (a) Mn valence of pristine $BaIr_{1-x}Mn_xO_3$ (x = 0.1, 0.2, and 0.3), Mn, $MnCO_3$, Mn_2O_3 and $BaMnO_3$ as a function of the photon energy for the Mn K-edge peak The Mn absorption edge of x = 0.1 does not show any energy shift with respect to $BaMnO_3$. Therefore, the valence of Mn is 4+ for x = 0.1, and the oxygen vacancy is negligible. On the other hand, the Mn absorption edge of x = 0.2 and 0.3 shows visible energy shift toward Mn_2O_3 with respect to $BaMnO_3$. Therefore, the valence of Mn is a mixture of 3+ and 4+ for x = 0.2 and 0.3, and oxygen vacancies exist to some extent. (b) Fourier transformed k^3-weighted Mn K-edge EXAFS for pristine $BaIr_{1-x}Mn_xO_3$ (x = 0.1, 0.2, and 0.3) in the representation form of $|X(R)|$.

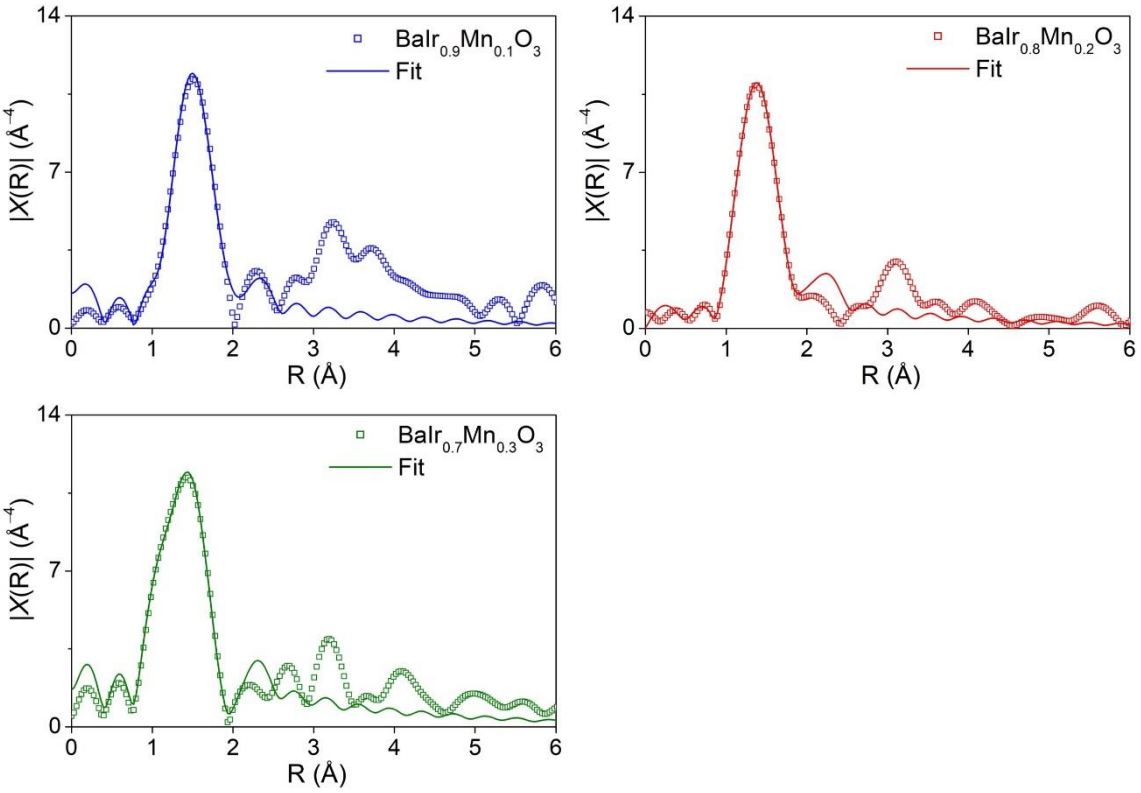

Fig. S8. Fourier transformed k^3-weighted Mn K-edge EXAFS fitting for pristine $BaIr_{1-x}Mn_xO_3$ (x = 0, 0.1, 0.2, and 0.3) in the representation form of $|X(R)|$. First and second shell was applied for the fitting. The fitting range was 2.7−10.7 $Å^{-1}$ in k-space, and 1.1−2.0 Å in R-space, respectively.

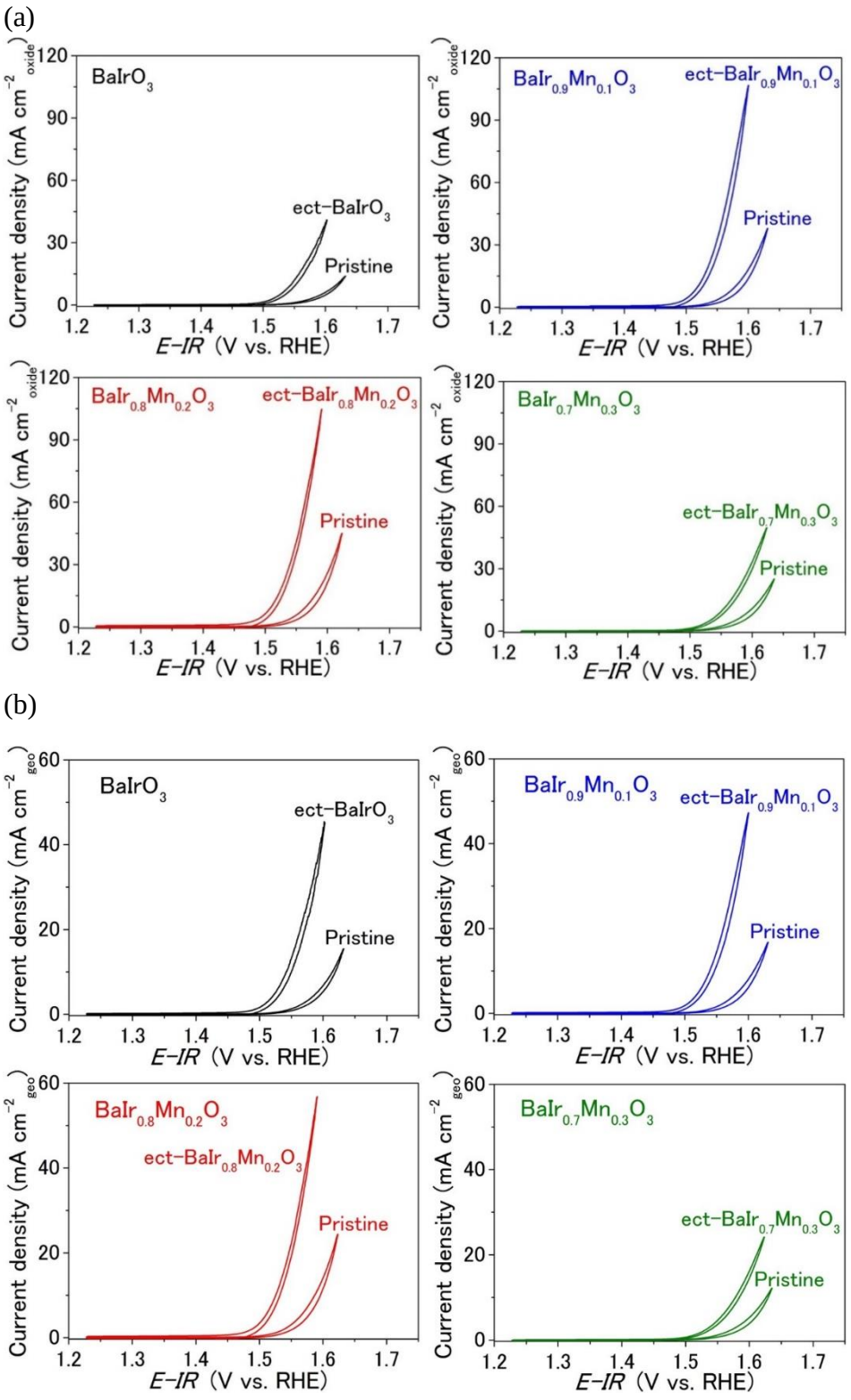

Fig. S9. The cyclic voltammograms for pristine and electrochemically treated (ect-) $BaIr_{1-x}Mn_xO_3$ (x = 0, 0.1, 0.2, and 0.3) normalized to (a) the oxide surface area and (b) the geometrical electrode area in in 0.5 M H_2SO_4 aqueous solution.

(a)

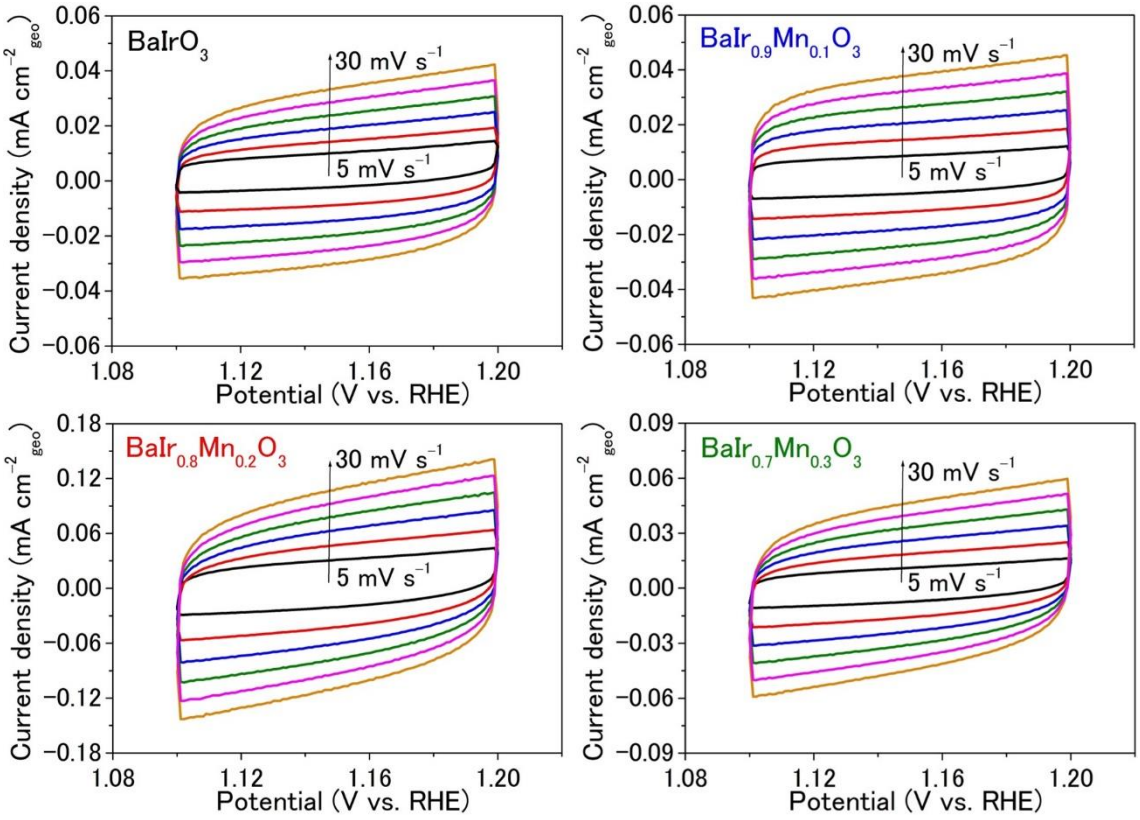
BaIrO3
BaIr0.9Mn0.1O3
BaIr0.8Mn0.2O3
BaIr0.7Mn0.3O3
30 mV s−1
5 mV s−1
Current density (mA cm−2geo)
Potential (V vs. RHE)

(b)

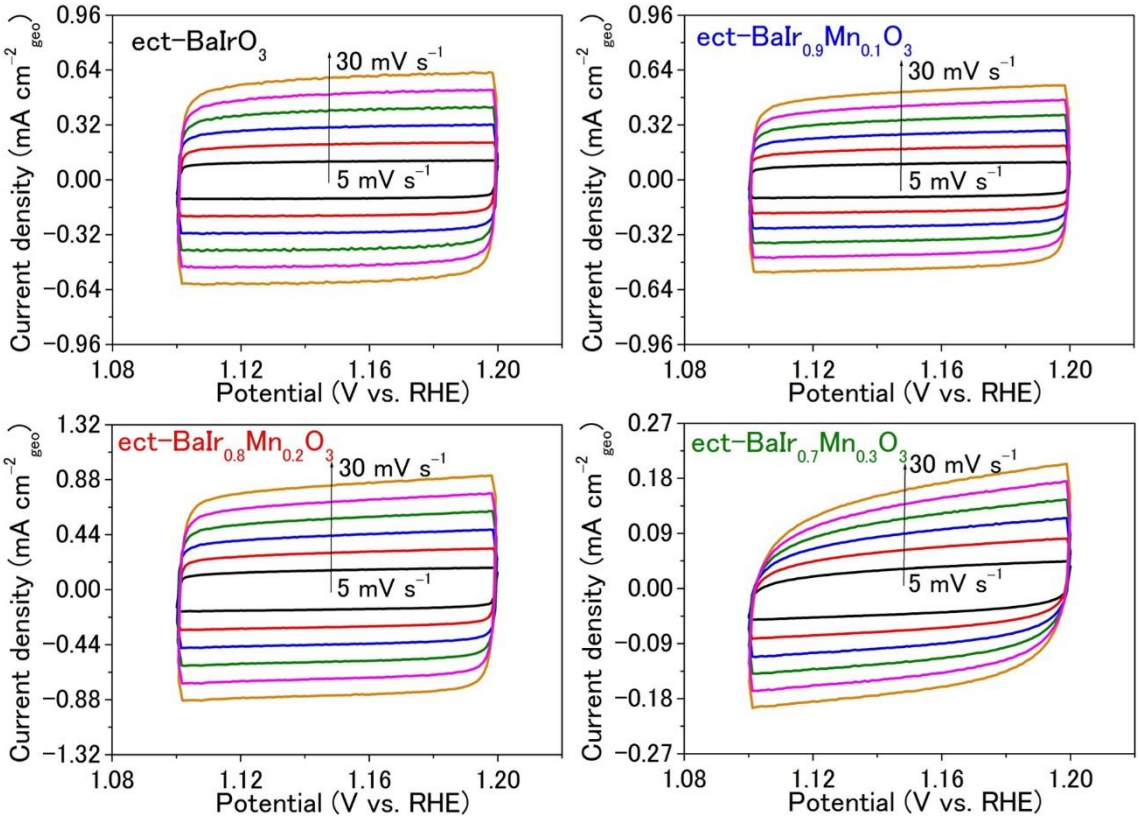
ect-BaIrO3
ect-BaIr0.9Mn0.1O3
ect-BaIr0.8Mn0.2O3
ect-BaIr0.7Mn0.3O3
30 mV s−1
5 mV s−1
Current density (mA cm−2geo)
Potential (V vs. RHE)

(c)

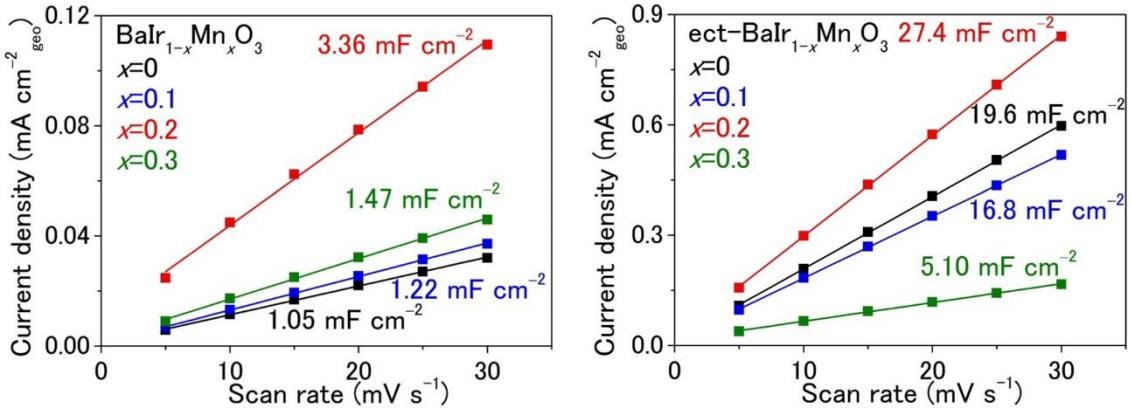

Fig. S10. Calculation of the double layer capacitance for $BaIr_{1-x}Mn_xO_3$. (a) The cyclic voltammograms for pristine $BaIr_{1-x}Mn_xO_3$ (x = 0, 0.1, 0.2, and 0.3) measured from 0.402−0.502 V vs. Hg/Hg_2SO_4 at the scan rate of 5−30 mV s^{-1} in 0.5 M H_2SO_4 aqueous solution. (b) The cyclic voltammograms for electrochemically treated (ect-) $BaIr_{1-x}Mn_xO_3$ (x = 0, 0.1, 0.2, 0.3) measured from 0.402-0.502 V vs. Hg/Hg_2SO_4 at the scan rate of 5−30 mV s^{-1} in 0.5 M H_2SO_4 aqueous solution. (c) The scan rate dependence of the current density at 1.15 V vs. RHE for pristine and electrochemically treated (ect-) $BaIr_{1-x}Mn_xO_3$ (x = 0, 0.1, 0.2, and 0.3). The slope of Fig. S10c corresponds to double layer capacitance (C_{dl}) per disk electrode area. Since the chemical composition is similar in pristine and electrochemically treated samples, the ideal specific capacitance (C_s) remains almost constant within each $BaIr_{1-x}Mn_xO_3$ (x = 0, 0.1, 0.2, and 0.3). Therefore, the electrochemically active surface area (ECSA) defined by $ECSA = C_{dl} / C_s$ [S1] is proportional to C_{dl} within each $BaIr_{1-x}Mn_xO_3$ (x = 0, 0.1, 0.2, and 0.3).

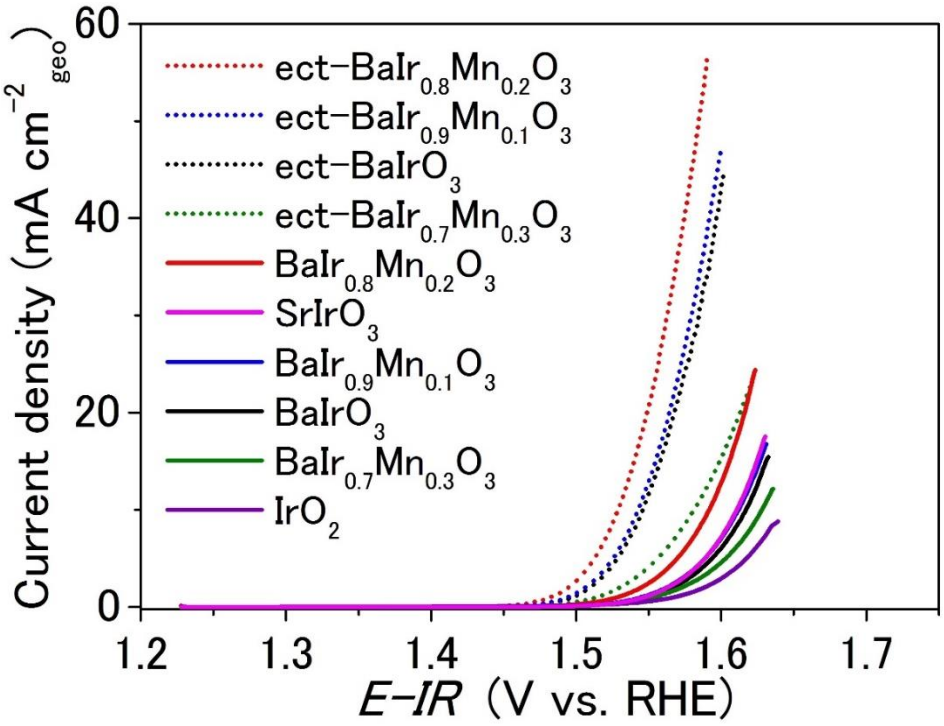

Fig. S11. The OER catalytic activity of $BaIr_{1-x}Mn_xO_3$. The linear sweep voltammograms for pristine and electrochemically treated (ect-) $BaIr_{1-x}Mn_xO_3$ (x = 0, 0.1, 0.2, and 0.3) in 0.5 M H_2SO_4 aqueous solution normalized to the geometrical electrode area (0.2 × 0.2 × π cm^2). Linear sweep voltammograms of IrO_2 and $SrIrO_3$ are shown for comparison.

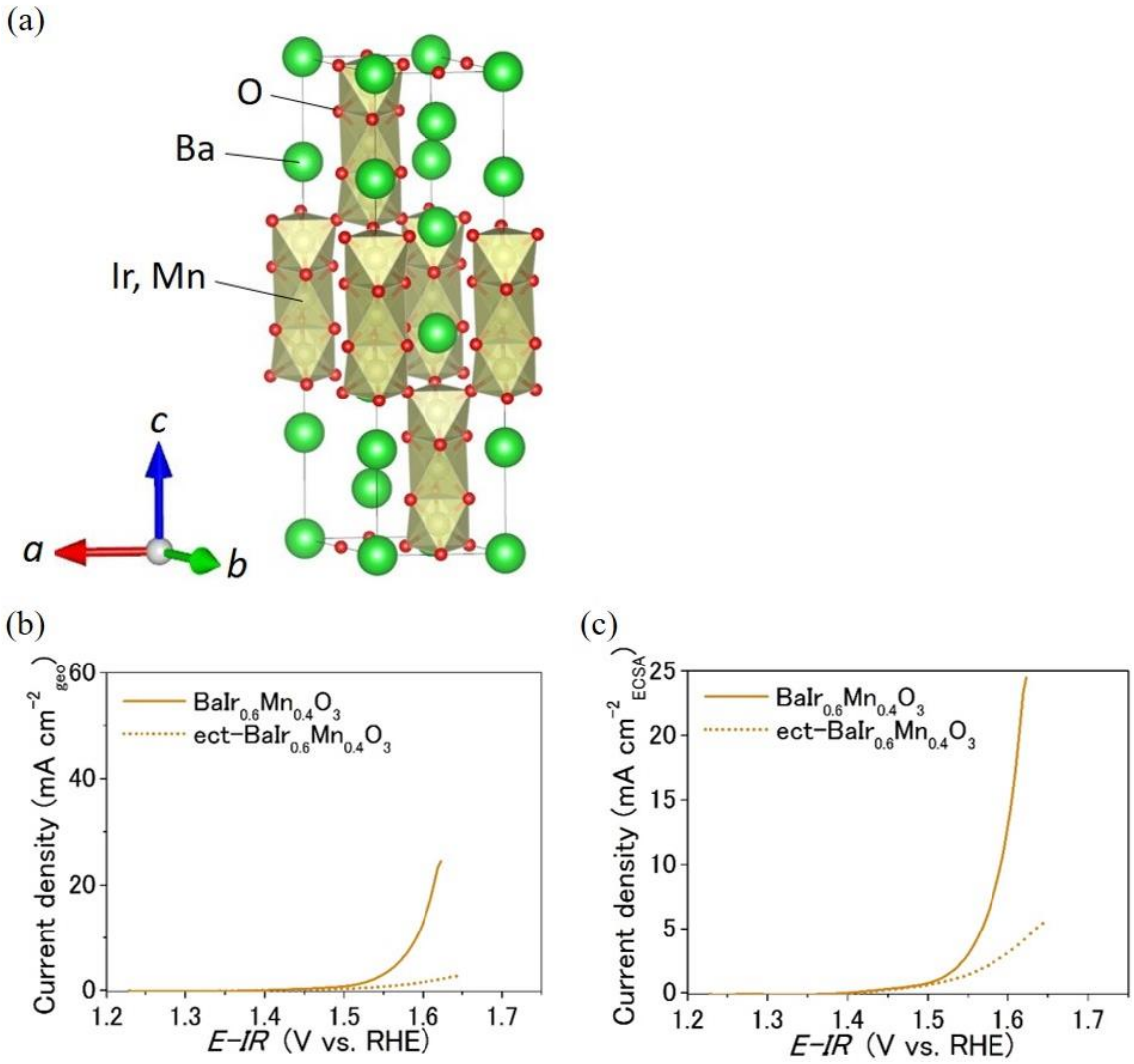

Fig. S12. Crystal structure and OER catalytic activity of $BaIr_{0.6}Mn_{0.4}O_3$. (a) Schematic representation of the crystal structure of $BaIr_{0.6}Mn_{0.4}O_3$. $BaIr_{0.6}Mn_{0.4}O_3$ adopts a hexagonal structure with the space group of *R*−3*mH*, which is characterized by the ionic coordination denoted as '9R'and it is isostructural with $BaRuO_3$ [33]. (b) The linear sweep voltammograms for pristine and electrochemically treated (ect-) $BaIr_{0.6}Mn_{0.4}O_3$ in 0.5 M H_2SO_4 aqueous solution normalized to the geometrical electrode area ($0.2 \times 0.2 \times \pi$ cm^2). (c) The linear sweep voltammograms for pristine and electrochemically treated (ect-) $BaIr_{0.6}Mn_{0.4}O_3$ in 0.5 M H_2SO_4 aqueous solution normalized to the relative ECSA. The relative ECSA is defined by the ratio of (ECSA of electrochemically treated $BaIr_{0.6}Mn_{0.4}O_3$)/(ECSA of pristine $BaIr_{0.6}Mn_{0.4}O_3$).

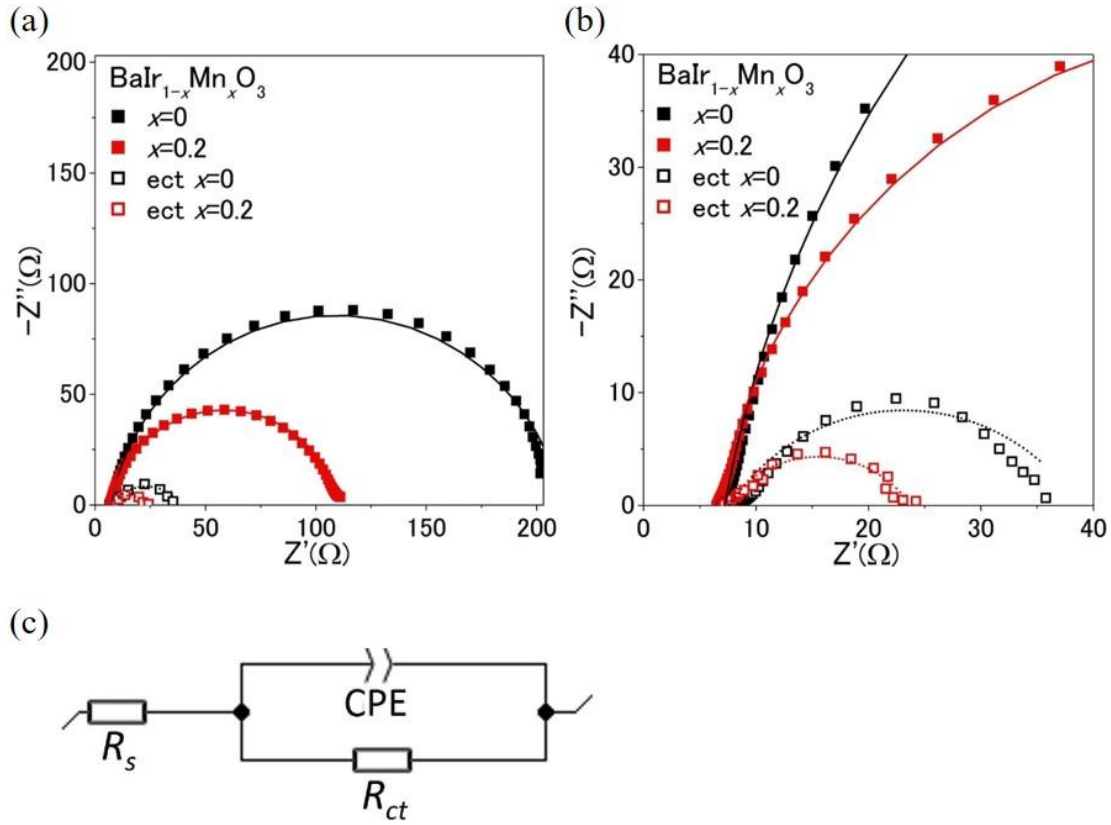

Fig. S13. The electrochemical impedance spectra of $BaIr_{1-x}Mn_xO_3$. (a) Nyquist plots for pristine and electrochemically treated (ect-) $BaIr_{1-x}Mn_xO_3$ (x =0 and 0.2) at 0.85−0.9 V vs. Hg/Hg_2SO_4 with an internal solution of 0.5 M H_2SO_4 (1.548−1.598 V vs. RHE) measured in the frequency range between 200 kHz and 100 mHz at the amplitude of 10 mV. (b) Expansion of Nyquist plots for pristine and electrochemically treated $BaIr_{1-x}Mn_xO_3$ (x =0 and 0.2). (c) The equivalent circuit used for fitting the EIS. R_s, R_{ct} and CPE denote the solution resistance, the charge transfer resistance and the constant phase element, respectively.

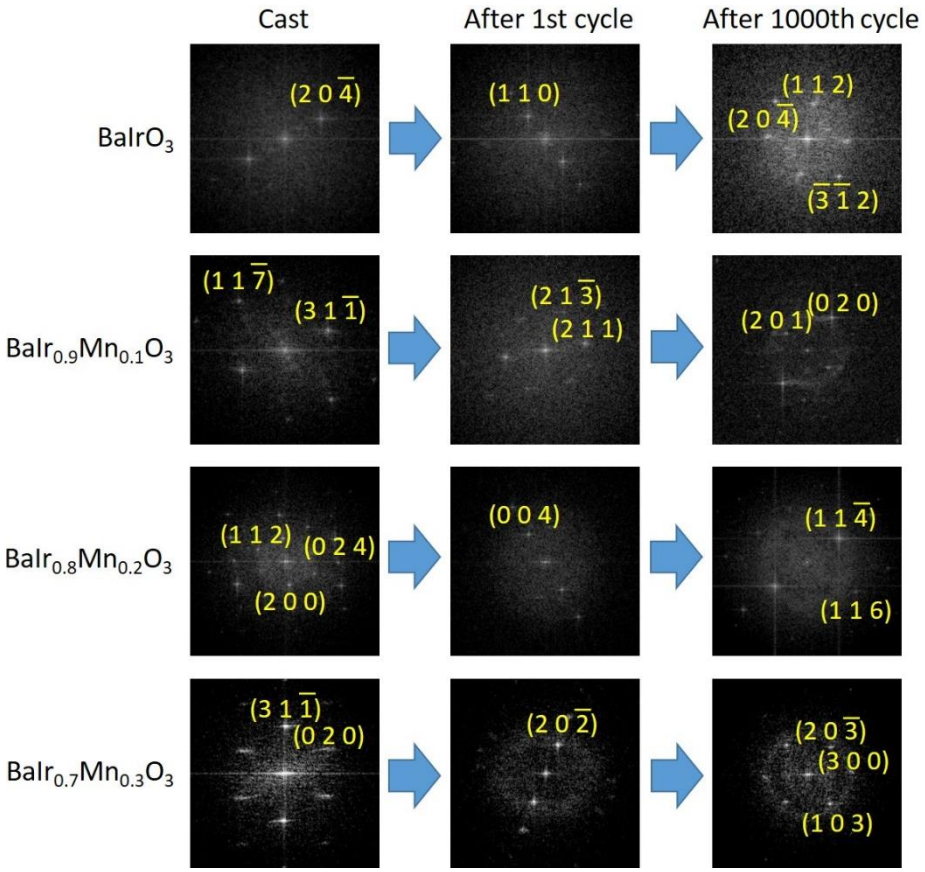

Fig. S14. Expansion of fast Fourier transform (FFT) images of $BaIr_{1-x}Mn_xO_3$. FFT images of as-cast, after 1st and 1000 OER cycles for $BaIr_{1-x}Mn_xO_3$ (x = 0, 0.1, 0.2, and 0.3) are shown. All the FFT images were obtained from the surface regions of 10 x 10 nm^2.

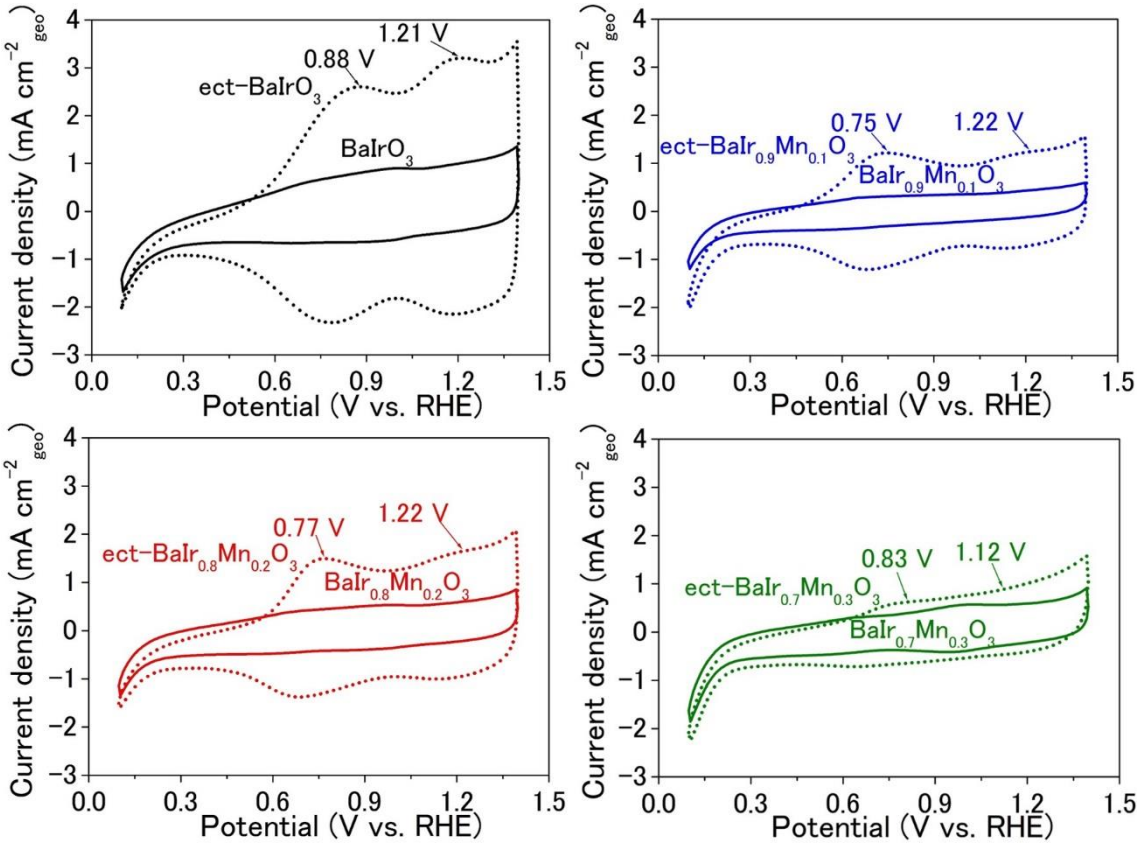

Fig. S15. The redox behavior of $BaIr_{1-x}Mn_xO_3$. The cyclic voltammograms for pristine and electrochemically treated (ect-) $BaIr_{1-x}Mn_xO_3$ (x = 0, 0.1, 0.2, and 0.3) measured from −0.6−0.7 V vs. Hg/Hg_2SO_4 at the scan rate of 100 mVs^{-1} in 0.5 M H_2SO_4 aqueous solution. The arrows in the figure demonstrate the Ir oxidation peak potential for $BaIr_{1-x}Mn_xO_3$. The first Ir oxidation peak of $BaIr_{1-x}Mn_xO_3$ originating from the oxidation from Ir^{3+} to Ir^{4+} appears at a lower potential than that of $BaIrO_3$, which indicates that Mn is a redox-inactive element for the Ir^{3+}/Ir^{4+} redox couple. The second Ir oxidation peak of $BaIr_{1-x}Mn_xO_3$ originating from the oxidation from Ir^{4+} to Ir^{5+} appears at a lower (x=0.3) or almost the same potential (x=0.1 and 0.2) in comparison with $BaIrO_3$, which indicates that Mn is also a redox-inactive element for the Ir^{4+}/Ir^{5+} redox couple. Therefore, Ir^{4+} is partially oxidized to Ir^{5+} during the OER mainly due to the Ir-site dissolution in $BaIr_{1-x}Mn_xO_3$ (and not because of the valence change of Mn).

(a)

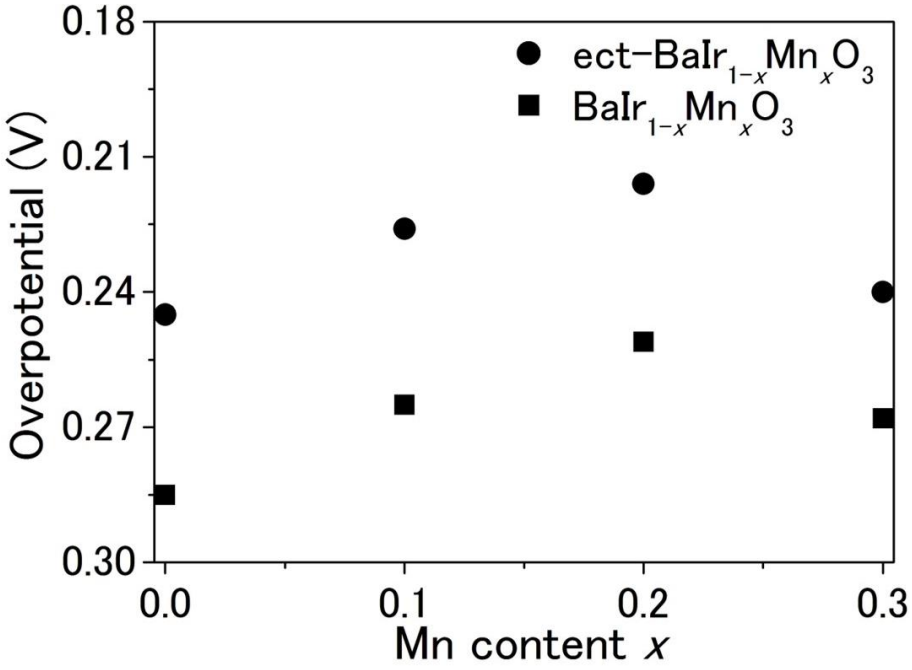

(b)

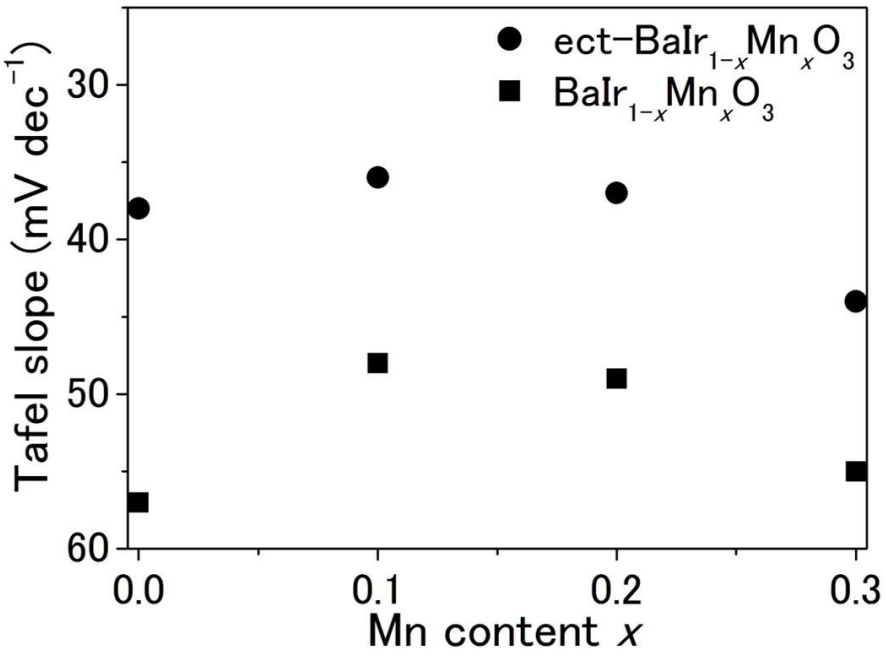

Fig. S16. Overpotential and Tafel slope of $BaIr_{1-x}Mn_xO_3$. (a) The relationship between the Mn content x and the overpotential (at 0.2 mA/cm^2) of pristine and electrochemically treated (ect-) $BaIr_{1-x}Mn_xO_3$ (x = 0, 0.1, 0.2, and 0.3). The overpotential (η) was determined from the onset potential (E_{onset}) by $\eta = E_{onset} - 1.23$ V. (b) The relationship between the Mn content x and the Tafel slope of pristine and electrochemically treated (ect-) $BaIr_{1-x}Mn_xO_3$ (x = 0, 0.1, 0.2, and 0.3).

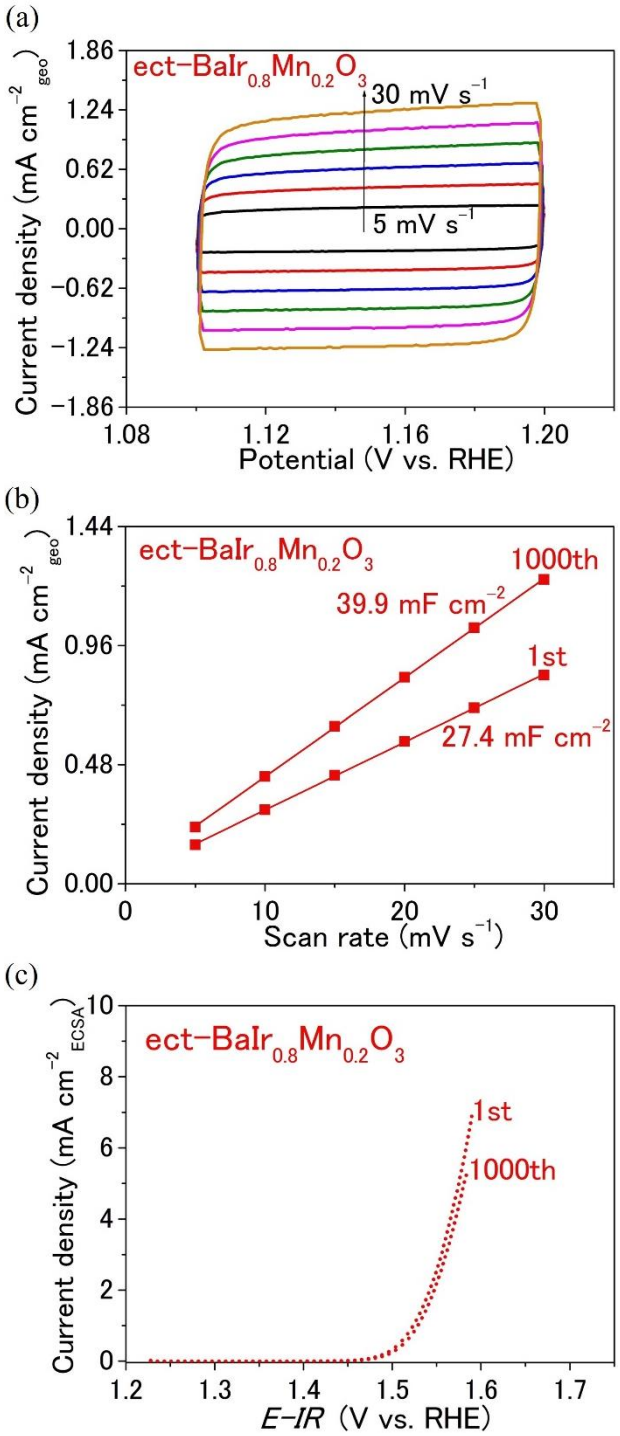

Fig. S17. Double layer capacitance and intrinsic activity for $BaIr_{0.8}Mn_{0.2}O_3$. (a) The cyclic voltammograms for electrochemically treated (ect-) $BaIr_{0.8}Mn_{0.2}O_3$ after additional 1000 OER cycles. (b) The scan rate dependence of the current density at 1.15 V vs. RHE for electrochemically treated (ect-) $BaIr_{0.8}Mn_{0.2}O_3$ after additional 1000 OER cycles. (c) The cycle dependence of the linear sweep voltammograms for electrochemically treated (ect-) $BaIr_{0.8}Mn_{0.2}O_3$ normalized to the relative ECSA with respect to pristine $BaIr_{0.8}Mn_{0.2}O_3$.

Table S1. Crystallographic results for $BaIr_{1-x}Mn_xO_3$. Lattice constants for x=0, 0.1, 0.2, and 0.3 were obtained by conducting Rietveld refinement on the XRD profile starting from the crystal structure of $BaIrO_3$ in JCPDS #01-080-1880. Ir-O bond distances, coordination number, and Bond Valence Sum (BVS) [S2] of Ir site were obtained by conducting extended X-Ray absorption fine structure (EXAFS) analysis. All these samples adopt the space group of *C*12/*m*1. The lattice constants are in good agreement with the previous study of $BaIr_{1-x}Mn_xO_3$ [S3]. Normalized lattice parameters, a_N, b_N, and c_N were calculated by $a_N = a/\sqrt{6}$, $b_N = b/\sqrt{2}$, $c_N = c(\sin\beta)/2\sqrt{3}$ on the basis of pseudo-cubic perovskite form as in the previous study of $BaIr_{1-x}Mn_xO_3$ [S3]. The decrease in Ir-O distance or the increase in coordination number corresponds to the stronger bonding of Ir-O. Ir $_{BVS}$ denote the Ir-O bond valence sum around Ir. The bond valence sum of $BaIr_{1-x}Mn_xO_3$ (x=0.1, 0.2, and 0.3) does not show any shift before and after the OER (even after 1000 OER cycles).

Material	$BaIrO_3$	$BaIr_{0.9}Mn_{0.1}O_3$	$BaIr_{0.8}Mn_{0.2}O_3$	$BaIr_{0.7}Mn_{0.3}O_3$
a (Å)	10.0032 (3)	9.9519(2)	9.9486(3)	9.9341(4)
b (Å)	5.7567(2)	5.7318(2)	5.7338(2)	5.7292(1)
c (Å)	15.1693(6)	15.0350(7)	14.9467(6)	14.8548(6)
V (Å^3)	850.28(4)	834.98(4)	830.28(3)	823.06(5)
Z (formula units)	12	12	12	12
a_N (Å)	4.0838(1)	4.0629(1)	4.0615(1)	4.0556(2)
b_N (Å)	4.0706(1)	4.0530(1)	4.0544(1)	4.0511(1)
c_N (Å)	4.2624(2)	4.2256(2)	4.2017(2)	4.1746(2)
V_N (Å^3)	70.857(3)	69.582(3)	69.190(3)	68.588(4)
β (deg.)	103.250(3)	103.199(4)	103.132(4)	103.216(4)
<Ir-O> (Å)	2.024(8)	2.022(11)	2.022(8)	2.018(9)
<Ir-O> of Ect (Å)	2.064(13)	2.020(10)	2.000(12)	2.032(23)
Coordination number	6 (fixed)	5.9(3)	6.0(2)	6.2(3)
Coordination of Ect	5.5(9)	5.9(3)	5.7(4)	6.7(7)
Ir $_{BVS}$	4.0	3.9(2)	4.0(1)	4.1(2)
Ir $_{BVS}$ of Ect	3.3(5)	3.9(2)	4.0(3)	4.3(4)
χ^2	8.88	9.78	8.58	7.13
R_{wp}	0.0954	0.1186	0.1123	0.0965

Table S2. BET Surface area of $BaIr_{1-x}Mn_xO_3$, $SrIrO_3$, and IrO_2. The specific surface area A_s was determined by krypton BET surface area measurements at 77 K using a surface area analyzer (BELSORP-max II, BEL Japan Inc., Japan).

Material	A_s (m^2/g)
$BaIrO_3$	0.87
$BaIr_{0.9}Mn_{0.1}O_3$	0.35
$BaIr_{0.8}Mn_{0.2}O_3$	0.43
$BaIr_{0.7}Mn_{0.3}O_3$	0.38
$SrIrO_3$	1.6
IrO_2	0.66

Table S3. The resistance elements of the equivalent circuit for pristine and electrochemically treated $BaIr_{1-x}Mn_xO_3$. These results were obtained by fitting the electrochemical impedance spectra (EIS) of (a) x=0 and (b) x=0.2 with the equivalent circuit in Fig. S13c. R_s and R_{ct} denote the solution resistance and the charge transfer resistance, respectively.

(a) Pristine x=0

E vs. Hg/Hg_2SO_4 (V)	R_s (Ω)	R_{ct} (Ω)
0.85	7	2800
0.9	7	204

(b) Pristine x=0.2

E vs. Hg/Hg_2SO_4 (V)	R_s (Ω)	R_{ct} (Ω)
0.85	7	554
0.9	7	103

(c) Electrochemically treated x=0

E vs. Hg/Hg_2SO_4 (V)	R_s (Ω)	R_{ct} (Ω)
0.85	7	180
0.9	8	31

(d) Electrochemically treated x=0.2

E vs. Hg/Hg_2SO_4 (V)	R_s (Ω)	R_{ct} (Ω)
0.85	7	37
0.9	7	16

Table S4. The turnover frequency (TOF) of OER for $BaIr_{1-x}Mn_xO_3$, $SrIrO_3$ and IrO_2. TOF was calculated by TOF = $J/4Fn$, where J is the OER current at 1.58 V vs. RHE, F is the Faraday constant, and n is the number of moles of the Ir atom on the working electrode.

Material	TOF (s^{-1})
Electrochemically treated $BaIrO_3$	0.207
Electrochemically treated $BaIr_{0.9}Mn_{0.1}O_3$	0.264
Electrochemically treated $BaIr_{0.8}Mn_{0.2}O_3$	0.465
Electrochemically treated $BaIr_{0.7}Mn_{0.3}O_3$	0.121
Pristine $BaIrO_3$	0.0248
Pristine $BaIr_{0.9}Mn_{0.1}O_3$	0.0327
Pristine $BaIr_{0.8}Mn_{0.2}O_3$	0.0727
Pristine $BaIr_{0.7}Mn_{0.3}O_3$	0.0313
Electrochemically treated $SrIrO_3$	0.0190
Pristine $SrIrO_3$	0.0214
IrO_2	0.00426

Table S5. Inductively coupled plasma optical emission spectroscopy (ICP-OES) results of $BaIr_{1-x}Mn_xO_3$. The elemental concentration of Ba, Ir and Mn in 0.5 M H_2SO_4 aqueous solution after 1st and 1000 OER cycles was determined by inductively coupled plasma (ICP, SHIMADZU ICPE-9000). ND denotes that the elemental concentration is below the detection limit. The detection limit of Ba, Ir, and Mn are 0.5 ppb, 5 ppb, and 0.2 ppb, respectively. The catalyst mass was ~32 μg and the 0.5 M H_2SO_4 electrolyte volume was 70 mL. Ba concentration of 1ppb corresponds to ~0.5 % of Ba mass in the catalyst.

Material	$BaIrO_3$	$BaIr_{0.9}Mn_{0.1}O_3$	$BaIr_{0.8}Mn_{0.2}O_3$	$BaIr_{0.7}Mn_{0.3}O_3$
Ba (after 1st cycle)	ND	ND	ND	ND
Ba (after 1000 cycles)	ND	1 ppb	0.8 ppb	0.8 ppb
Ir (after 1st cycle)	ND	ND	ND	ND
Ir (after 1000 cycles)	ND	ND	ND	ND
Mn (after 1st cycle)	-	ND	ND	ND
Mn (after 1000 cycles)	-	ND	ND	ND

Supplementary References

[S1] C. C. L. McCrory, S. H. Jung, J. C. Peters and T. F. Jaramillo, *J. Am. Chem. Soc.*, 2013, **135**, 16977-16987.

[S2] I. D. Brown and D. Altermatt, *Acta Cryst.*, 1985, **B41**, 244-247.

[S3] J. G. Zhao, L. X. Yang, Y. Yua, F. Y. Li, R. C. Yu and C. Q. Jin, *J. Solid State Chem.*, 2010, **183**, 720-726.